



**HAL**  
open science

## Field-Aligned Potentials at Mars From MAVEN Observations

Shaosui Xu, David L. Mitchell, James P. Mcfadden, Glyn Collinson, Yuki Harada, Robert Lillis, Christian Mazelle, J. E. P. Connerney

► **To cite this version:**

Shaosui Xu, David L. Mitchell, James P. Mcfadden, Glyn Collinson, Yuki Harada, et al.. Field-Aligned Potentials at Mars From MAVEN Observations. *Geophysical Research Letters*, 2018, 45, pp.10,119-10,127. 10.1029/2018GL080136 . insu-03678176

**HAL Id: insu-03678176**

**<https://insu.hal.science/insu-03678176>**

Submitted on 25 May 2022

**HAL** is a multi-disciplinary open access archive for the deposit and dissemination of scientific research documents, whether they are published or not. The documents may come from teaching and research institutions in France or abroad, or from public or private research centers.

L'archive ouverte pluridisciplinaire **HAL**, est destinée au dépôt et à la diffusion de documents scientifiques de niveau recherche, publiés ou non, émanant des établissements d'enseignement et de recherche français ou étrangers, des laboratoires publics ou privés.

Copyright

## RESEARCH LETTER

10.1029/2018GL080136

## Key Points:

- This study provides a statistical analysis of field-aligned potentials at Mars, which we attribute to the ambipolar electric field
- The potential difference between the ionospheric source region and the spacecraft ranges from 0 to 1.5 V with **E** directing away from Mars
- Derived dayside electric fields are <3 mV/km and located near the ion exobase, where they are most effective at enhancing ion outflow

## Supporting Information:

- Supporting Information S1

## Correspondence to:

S. Xu,  
shaosui.xu@ssl.berkeley.edu

## Citation:

Xu, S., Mitchell, D. L., Mcfadden, J. P., Collinson, G., Harada, Y., Lillis, R., et al. (2018). Field-aligned potentials at Mars from MAVEN observations. *Geophysical Research Letters*, 45, 10,119–10,127. <https://doi.org/10.1029/2018GL080136>

Received 20 AUG 2018

Accepted 19 SEP 2018

Accepted article online 24 SEP 2018

Published online 4 OCT 2018

Corrected 16 OCT 2018

This article was corrected on 16 OCT 2018. See the end of the full text for details.

## Field-Aligned Potentials at Mars From MAVEN Observations

Shaosui Xu<sup>1</sup> , David L. Mitchell<sup>1</sup> , James P. McFadden<sup>1</sup>, Glyn Collinson<sup>2</sup> , Yuki Harada<sup>3,4</sup> , Robert Lillis<sup>1</sup> , Christian Mazelle<sup>5</sup> , and J. E. P. Connerney<sup>2</sup> 

<sup>1</sup>Space Sciences Laboratory, University of California, Berkeley, CA, USA, <sup>2</sup>Goddard Space Flight Center, Greenbelt, MD, USA, <sup>3</sup>Department of Physics and Astronomy, University of Iowa, Iowa City, IA, USA, <sup>4</sup>Department of Geophysics, Kyoto University, Kyoto, Japan, <sup>5</sup>IRAP, CNRS-University of Toulouse-UPS-CNES, Toulouse, France

**Abstract** One possible ion escape channel at Mars is a polar wind-like outflow driven by parallel electric fields and/or other acceleration mechanisms. With independent potential estimates from ionospheric photoelectron measurements by the Solar Wind Electron Analyzer (SWEA) and ion measurements by the SupraThermal And Thermal Ion Composition (STATIC) onboard the Mars Atmosphere and Volatile Evolution (MAVEN) spacecraft, magnetic field-aligned potentials are calculated as the difference of the two. The calculated field-aligned potentials have average values that range from 0 to  $-1.5$  V, relative to the ionospheric source region. These field-aligned potentials likely result from ambipolar electric fields and are found on both closed and open field lines. On the dayside, these potentials range from 0 to  $-0.7$  V, corresponding to an electric field magnitude  $<3$  mV/km, which peaks near the ion exobase and can effectively accelerate ions and enhance ion outflow.

**Plain Language Summary** The Mars Atmosphere and Volatile Evolution (MAVEN) mission is dedicated to studying atmospheric loss from Mars at the current epoch and estimating the total loss to space over Martian history. Atmospheric escape can be in the form of neutral particles and charged particles (i.e., ions and electrons). Charged particles subject to electromagnetic forces at Mars. Ions, more gravitationally bounded than electrons, can be accelerated to escape velocities by these forces. One of the accelerating forces for ions at Mars is in the form of ambipolar electric field, produced by electron-ion separation. This study provides the first statistical analysis of ambipolar electric field at Mars with MAVEN data. Integrating this force over a spatial distance, the resulting potential, determined from MAVEN's measurements, ranges from 0 to  $-1.5$  eV. These potentials can accelerate more ions to escape velocity and enhance ion escape. This study is crucial to characterize low-energy ion escape, an important atmospheric loss channel.

## 1. Introduction

The Mars Atmosphere and Volatile Evolution (MAVEN) mission is dedicated to studying atmospheric loss from Mars at the current epoch and estimating the total loss to space over the Martian history (Jakosky et al., 2015, 2018). One ion escape channel is outflow along open field lines (e.g., Ergun et al., 2016; Lillis et al., 2015), enhanced by a polarization or ambipolar electric field, analogous to the polar wind at Earth (e.g., Banks & Holzer, 1968; Ganguli, 1996; Schunk, 1988; Welling et al., 2015; Yau et al., 2007). Because of their light mass, electrons outrun ions and set up an electric field to accelerate ions to counterbalance the charge separation. Traditionally, the ambipolar electric field (**E**) originates from the thermal electron pressure gradient (e.g., Schunk & Nagy, 2009); that is,

$$e\mathbf{E} = -\frac{\nabla p_e}{n_e}, \quad (1)$$

where  $p_e$  is the electron pressure,  $n_e$  is the electron density, and  $e$  is the fundamental charge. This term is an important mechanism for driving ion vertical diffusion (e.g., Schunk & Nagy, 2009). At Mars, the ambipolar electric field due to thermal electrons is typically on the order of  $\sim 1$  mV/km in the ionosphere, based on typical Martian electron density and temperature profiles. Other mechanisms are important for ion outflow at Earth (Yau et al., 2007, and references therein), such as wave-particle interaction, ion heating, and centrifugal force.

In the ionosphere, superthermal electrons ( $>1$  eV) usually have an insignificant density compared to the total thermal electron density, but their velocities are high ( $\sim 600$  km/s at 1 eV). It has been found that these

hot electrons can contribute significantly to the ambipolar electric field and enhance ion escape at Earth (e.g., Glocer et al., 2017; Khazanov et al., 1997, 1998; Kitamura et al., 2015) and Venus (e.g., Collinson, Frahm, et al., 2016).

Collinson et al. (2015) set an upper bound on the total potential drop in the ionosphere of Mars of  $\pm 2$  V by examining MAVEN data. However, a more accurate estimate of the magnitude of the ambipolar electric field at Mars is needed, which is the topic of this study. SupraThermal And Thermal Ion Composition (STATIC) (McFadden et al., 2015) and Solar Wind Electron Analyzer (SWEA; Mitchell et al., 2016) onboard MAVEN measure ions and electrons down to energies of  $\sim 0.1$  and  $\sim 3$  eV, respectively, which are significantly affected by the spacecraft potential as well as electrostatic potentials in the Mars environment. Negative potentials can be derived with SWEA and STATIC measurements via independent techniques. The method used for STATIC data in this study provides the spacecraft potential, whereas the method used for SWEA data provides the total potential (spacecraft + Mars environment). Therefore, Mars field-aligned potentials can be calculated from the difference between SWEA and STATIC estimates. We also use magnetic field data from the Magnetometer (Connerney et al., 2015) to determine electron pitch angles and directions, which allows us to infer magnetic topology.

## 2. Methodology: Negative Potentials From SWEA and STATIC

There are several techniques for estimating field-aligned potentials using electron measurements. Lillis et al. (2018) utilized the energy dependence of the electron loss cone size measured on open magnetic field lines to determine the strength and polarity of the potential difference between the observation altitude and the superthermal electron exobase ( $\sim 160$ -km altitude; Xu, Liemohn, Bougher, & Mitchell, 2015; Xu, Liemohn, et al., 2016) with Mars Global Surveyor data. Kitamura et al. (2012) and Collinson, Mitchell, et al. (2016) determined field-aligned potentials above the spacecraft by comparing outflowing photoelectron fluxes and precipitating electron fluxes at Earth and at Mars, respectively. Collinson, Frahm, et al. (2016) investigated “polar wind”-like ambipolar electric fields at Venus by examining photoelectron energy spectral features. With the same technique, Collinson et al. (2015) determined the upper bound on the total potential drop in the Martian ionosphere to be less than 2 V. The technique used in Lillis et al. (2018) only works for large field-aligned potentials (roughly  $> 10$  V). The technique adopted by Kitamura et al. (2012) and Collinson, Mitchell, et al. (2016) requires inflowing electron fluxes to be significantly lower than outflowing fluxes, which only occurs at Mars occasionally, and is only valid for potentials larger than the lowest measured energy (3 eV for SWEA). In this study, we aim to determine small field-aligned potentials (within  $\pm 2$  V) and thus can only use a technique similar to that of Collinson et al. (2015) and Collinson, Frahm, et al. (2016).

### 2.1. Potential Estimates From SWEA

We estimate potentials with SWEA by measuring shifts in the positions of discrete features in ionospheric photoelectron energy spectra. At Mars, peaks in the photoelectron spectrum at  $\sim 23$  and 27 eV are caused by the ionization of  $\text{CO}_2$  and/or O by the intense 30.4-nm solar He-II emission line (e.g., Liemohn et al., 2003; Mantas & Hanson, 1979; Mitchell et al., 2000; Peterson et al., 2016; Xu & Liemohn, 2015; Xu, Liemohn, Peterson, et al., 2015; Xu, Thiemann, et al., 2018). Whenever ionospheric photoelectrons are observed by SWEA, these peaks are shifted in the instrument frame by both the spacecraft and Mars potentials. The Mars potential is the potential difference between the ionospheric source region and the spacecraft location. The spacecraft potential is the potential between the conducting part of the spacecraft (to which the instruments are grounded) and the ambient plasma many Debye lengths ( $\sim 1$  cm to tens of meters) from the spacecraft. We designed an automated procedure to calculate the energy shift of a sharp feature in the primary photoelectron energy spectrum at 23 eV.

SWEA has an energy resolution of  $\Delta E/E = 16.7\%$  for the burst-mode pitch angle distribution (PAD) data (33.4% for the survey-mode PAD data, which averages adjacent energy steps in the sweep). If we estimate the measurement accuracy to be half of the energy bin width, the accuracy improves as the total potential difference from the ionosphere source region to the spacecraft becomes larger, and the 23-eV peak is shifted to lower energies in the instrument frame where  $\Delta E$  is smaller. It is also important to note that this technique is based on ionospheric photoelectron observations, thus indicating that these electrons are on magnetic field lines intersecting the dayside ionosphere (e.g., Xu, Fang, et al., 2018; Xu, Mitchell, Liemohn, et al., 2017; Xu, Mitchell, Luhmann, et al., 2017): (1) closed field lines (two foot points embedded in the dayside ionosphere), (2) open field lines (one foot point embedded in the ionosphere and the other connected to solar wind),

or (3) cross-terminator closed field lines (one foot point embedded in the dayside ionosphere and the other foot point embedded in the nightside atmosphere).

### 2.2. Potential Estimates From STATIC

To obtain Mars potentials, we need an independent estimate of the spacecraft potential, which can be obtained with STATIC observations in two ways. Below 200-km altitude, the ion mean free path is  $< \sim 10$  km, so that acceleration between collisions by typical electric fields in the Mars environment ( $< \sim$  few mV/km) is insignificant compared to acceleration by the spacecraft potential, which typically has an amplitude of a few volts over a scale length of 1 cm. The spacecraft potential is estimated by assuming that the main ion species,  $O_2^+$ , has zero bulk velocity in the rotating Mars frame so that its ram energy is entirely due to the spacecraft velocity; any difference is caused by the spacecraft potential.

Above 300 km, the spacecraft potential is obtained by identifying a sharp low-energy cutoff in the ion energy distribution, which is established when the ions cross the negative spacecraft potential as they enter the STATIC aperture. We use light (mass  $< 10$  amu) ions for this purpose, since protons typically have much broader energy distributions than the spacecraft potential, and they also have broad angular distributions because of their low mass. This is important because small field-aligned potentials (such as those considered in this study) have much less effect on more perpendicular protons than on field-aligned protons so that when averaging over all angles, the low-energy cutoff is mostly likely not affected by field-aligned potentials. Between 200 and 300 km, the spacecraft potential is estimated as the less negative value from the two techniques. STATIC has an energy resolution of  $\Delta E/E = 16\%$  so that measurement accuracy decreases with more negative potentials, which accelerate ions to higher energies.

### 2.3. Cross-Calibration, Caveats, and Data Selection

Below the superthermal electron exobase ( $\sim 160$  km), photoelectrons have a small mean free path ( $< 10$  km) due to frequent collisions with neutrals and also local production of photoelectrons dominates so that they experience  $< 0.01$ -V potential for an electric field  $\sim 1$  mV/km (typical for an ambipolar electric field). We cross-calibrated the difference of SWEA and STATIC estimates to be nearly 0 on average below 160-km altitude to minimize the possible systematic bias in SWEA estimates due to uncertainties (SWEA's finite bin width) in locating the He-II peaks.

There are three caveats to our approach. (A) Both SWEA and STATIC potentials are only negative, which could result in incomplete sampling or a systematic bias in regions where spacecraft potential can be either positive or negative. (B) For STATIC estimates of the spacecraft potential below 200–300 km, the assumption of zero bulk flow velocity might not be valid and cause an underestimation or overestimation of the spacecraft potential, depending on the flow velocity relative to the spacecraft motion. Thermospheric winds near the exobase are typically in the range 200–300 m/s (e.g., Bougher et al., 2000, 2015), which could shift the ram energy by up to a few tenths of an electron volt. However, since the bulk flow direction can be at any angle with respect to ram, this energy shift should be averaged out with enough sampling. (C) If the ion distribution is shifted to higher energies, such that the wings of the distribution produce very few counts near the cutoff energy, then it is not possible to measure the cutoff, or it is possible to have a false potential estimate by misinterpreting low count rates in the wing of the distribution as the spacecraft potential cutoff.

We select SWEA and STATIC data from 1 December 2014 to 1 March 2018. To obtain the best accuracy, only SWEA burst-mode PAD data are used and only negative potentials are selected, which shift the He-II peaks to lower energies (smaller  $\Delta E$ ). STATIC has an instrumental issue at low energies, which is thought to be caused by exposure of the CuO-coated analyzer surfaces to atomic oxygen in the Mars environment. This exposure is nonuniform (more near the entrance aperture) and thus modifies the work function of the analyzer nonuniformly, which reduces its sensitivity at low energy. The effects of this low-energy “ion suppression” have been corrected for all data used in this study; however, the suppression was too large from 1 January to 1 November 2015 to allow a reliable correction. Therefore, we exclude STATIC potential estimates for this period when the bulk flow method is used. The proton cutoff method is not affected because of its broader angular distribution, which allows ions to enter the aperture from directions where the work function has not been modified. Lastly, caveat C poses a particular challenge to STATIC estimates based on the low-energy cutoff of protons in the sunlit flanks, where thermal plasma gains a significant flow velocity once past the obstacle of Mars. We impose an empirical data selection criterion in this region, excluding data with STATIC estimates  $< -1.5$  V. This is because, based on experience in the solar wind over a range of plasma densities, the potential is expected to be within a few volts of zero in this higher density sunlit plasma region and also that the distribution of

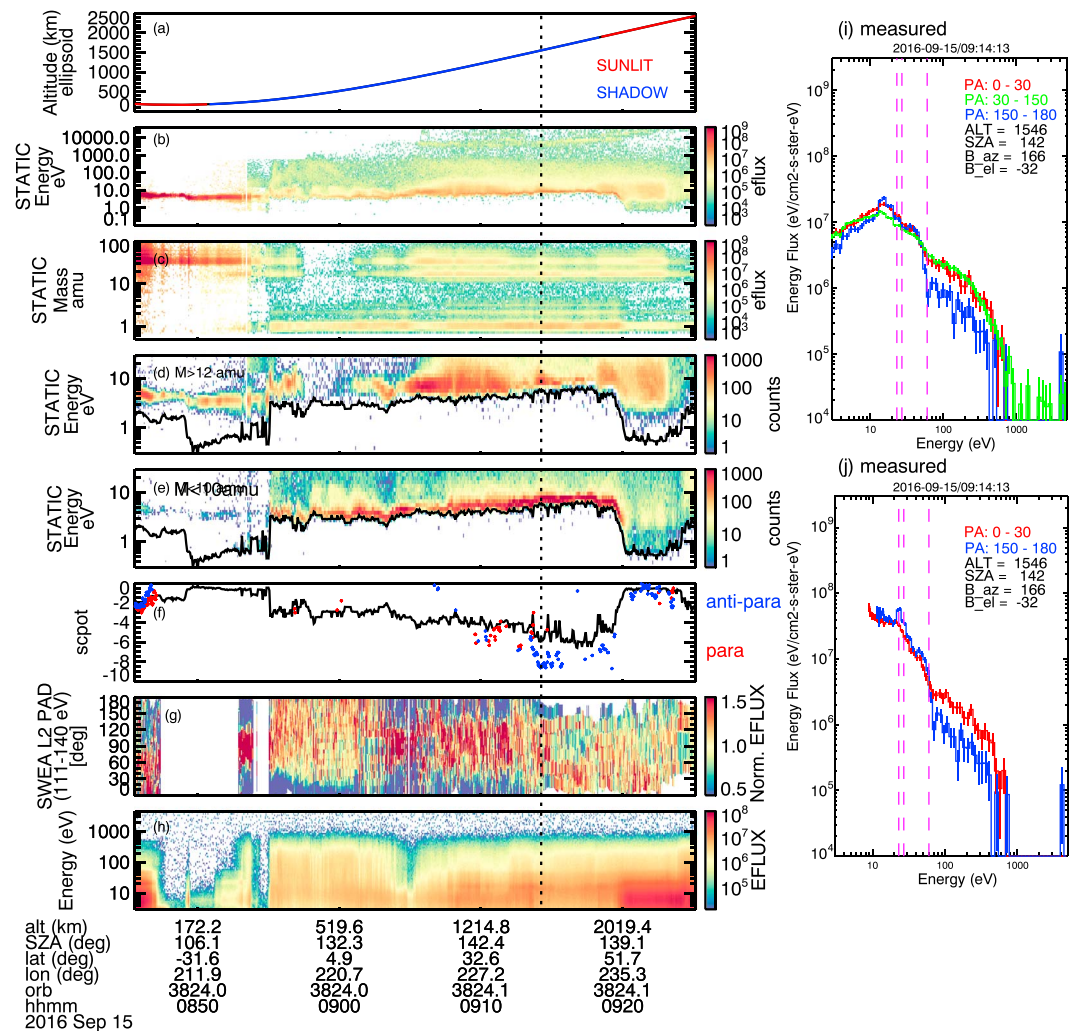


**Figure 1.** Time series of the spacecraft altitude (a), energy spectra for all masses (b), and mass spectra (c) measured by STATIC, STATIC energy spectra for heavy ions (d, >12 amu) and light ions (e, mass <10 amu), negative potentials (f), from SWEA and STATIC, electron pitch angle distributions (PADs) (g), and energy spectra (h) measured by SWEA on 15 September 2016. In panels (d) and (e), the black lines are absolute spacecraft potentials from STATIC measurements. In panel (f), the black solid line shows the negative spacecraft potentials from STATIC and red and blue dots are deduced negative potentials from SWEA measurements for electrons traveling parallel and antiparallel to magnetic fields, respectively. Panel (i) illustrates the measured electron energy spectra for three pitch angle (PA, in degrees) ranges, extracted at the time indicated by the vertical dashed line in the left panels. Panel (j) shows the blue and red energy spectra in panel (i) shifted for  $-8.5$  V (Mars + spacecraft potentials) and  $-6$  V (spacecraft potential only), respectively, by applying the Liouville's theorem. The vertical violet dashed lines in (i) and (j) indicate the locations of the He-II features at 23 and 27 eV and the photoelectron knee at 60 eV. STATIC = SupraThermal And Thermal Ion Composition; SWEA = Solar Wind Electron Analyzer; PAD = pitch angle distribution; SZA = solar zenith angle.

SWEA estimates is Gaussian-like for STATIC estimates between 0 and  $-1.5$  V but bimodal for STATIC estimates  $<-1.5$  V. Nonetheless, readers should treat results obtained in this region with caution.

### 3. Case Study

In this section, an orbit example is presented to demonstrate the methodology. Spacecraft potentials (absolute values) from STATIC (black lines in Figures 1d and 1e) track the low-energy cutoff in the distributions of light ions. In particular, right after 09:20 UT, STATIC estimates the spacecraft potential based on the low-energy cutoff of the light ions (Figure 1e), while heavy ions are accelerated and have a different apparent cutoff (Figure 1d). This demonstrates the importance of using low mass ions (mostly protons) to estimate the spacecraft potential. In Figure 1f, we overlay the signed STATIC potential estimates with SWEA potential estimates,

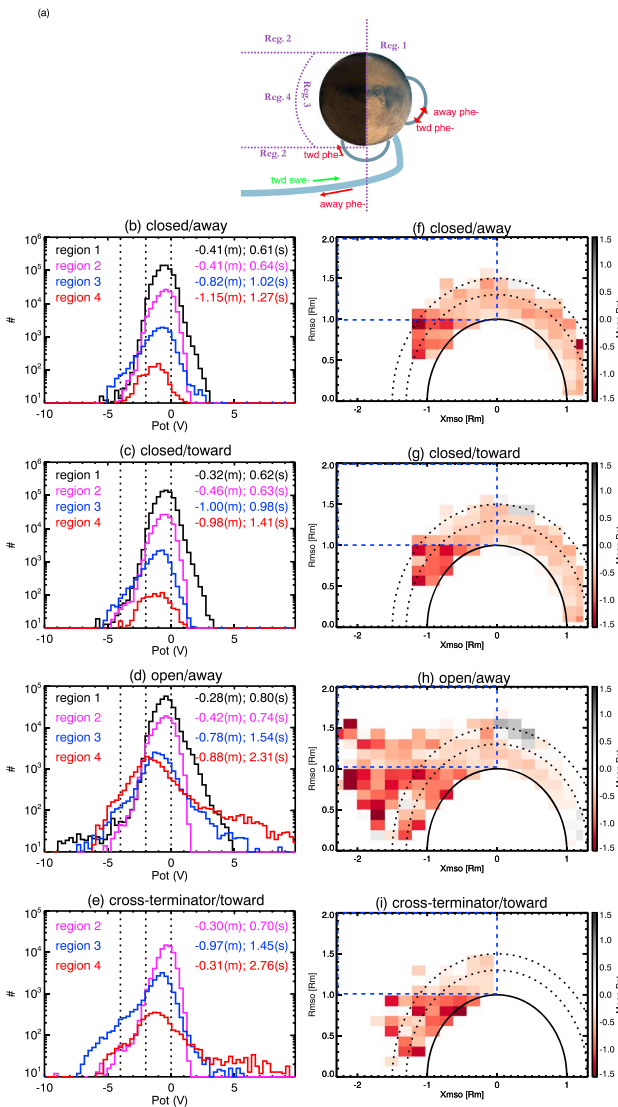


**Figure 2.** (a) A schematic shows three magnetic topologies that have photoelectrons on one or both field-aligned direction(s). The purple dotted lines separate four regions:  $X_{mso} > 0$  (Region 1),  $X_{mso} < 0$  and  $r_{mso} > 1 R_m$  (Region 2),  $X_{mso} < 0$ ,  $r_{mso} < 1 R_m$  and altitudes  $< 1,000$  km (Region 3), and  $X_{mso} < 0$ ,  $r_{mso} < 1 R_m$  and altitudes  $> 1,000$  km (Region 4), where  $r_{mso}$  is the distance from the  $X_{mso}$  axis and  $R_m$  is the Mars radius. Panels (b)–(e) show the histograms of Mars potentials for these four regions, highlighted by different colors. Panels (b, away) and (c, toward) are for closed field lines. Panel (d) are observations on an open field line. Panel (e) are observations on a cross-terminator closed field line. The two columns of numbers on the right in panels (b)–(e) are the mean values (m) and standard deviations (s) in each region. Panels (f)–(i) are the mean Mars potentials in the cylindrical MSO coordinates for topologies corresponding to panels (b)–(e). The blue dashed boxes in panels (f)–(i) highlight Region 2, where we applied an additional empirical data selection.

based on photoelectrons traveling parallel (red) and antiparallel (blue) to the magnetic field. In this example, we see the SWEA method yields potentials that are 2–4 V more negative than the STATIC potential estimates.

Consider the time marked by the vertical dashed line as an example. Figure 1i is a typical observation for an open field line: with photoelectrons traveling away from the planet (blue spectrum) and solar wind electrons precipitating onto the atmosphere (red spectrum; e.g., Xu et al., 2014; Xu, Mitchell, Liemohn, et al., 2017). The energy shift of the 23-eV photoelectron feature yields a potential of  $-8.5$  V, while the low-energy cutoff of the ion distribution at the same time gives a  $-6$ -V spacecraft potential. After correcting for both the Mars and spacecraft potentials the He-II feature in the blue spectrum is shifted to 23 eV (Figure 1j), as they would appear in the source region at the foot point of the magnetic field line. For this observation, the Mars field-aligned potential is determined to be  $-2.5$  V, from the ionospheric foot point to the spacecraft altitude.

## 4. Statistical Results

### 4.1. Distributions and Mapping of Mars Potentials

The case study above demonstrates how we calculate Mars potentials based on independent estimates from SWEA and STATIC, which is applied to all the selected data. SWEA potential estimates are calculated independently for electrons traveling “away from” or “toward” Mars, based on the orientation of the magnetic field combined with the electron PAD. Figure S1 in the supporting information maps potential estimates from SWEA (“away” and “toward”) and STATIC in the MSO (Mars-centered Solar Orbital) cylindrical coordinates. In the MSO coordinates,  $X$  points to the Sun;  $Y$  points opposite to Mars’ orbital angular velocity, and  $Z$  points to Mars’ north ecliptic pole. Mars potentials are obtained by taking the difference between SWEA and STATIC potential estimates. SWEA and STATIC potential estimates are both negative, but the difference between the two can be either positive or negative.

As mentioned above, SWEA potential estimates, and thus Mars potentials, rely on photoelectron observations, which also provide information on magnetic topology. With STATIC providing the spacecraft potential for every SWEA measurement, there are four situations: photoelectrons, and thus SWEA potential estimates, are (1) simultaneously detected in both the “away” and “toward” directions (relative to Mars), (2) only detected in the “away” direction, (3) only detected in the “toward” direction, and (4) not observed in either direction. Cases 1–3 correspond to three magnetic topologies that have access to dayside ionosphere: closed with both foot points on dayside, open, and cross-terminator closed field lines, respectively, as shown in Figure 2a.

For a dayside closed loop (case 1), Mars potentials are obtained separately for “away” photoelectrons and “toward” photoelectrons, corresponding to the potential difference from the corresponding foot point. Statistical analysis can be applied to each direction separately. For more negative potentials, the spectral feature that provides the spacecraft potential is

shifted to an energy with a smaller  $\Delta E$  for SWEA and a larger  $\Delta E$  for STATIC. As  $\Delta E/E \approx 16\%$  for both instruments, the uncertainty is typically 1–2 V, which is comparable to the calculated Mars potentials. To ensure that our method provides statistically significant estimates of the Mars potential, we plot distributions of the measured potentials for the “away” direction in Figures 2b and the “toward” direction in Figure 2c, with lines of different colors corresponding to the four spatial regions shown in Figure 2a.

For open field lines (case 2), photoelectrons can only be observed flowing away from Mars, with incident solar wind electrons. Therefore, the Mars potential can be only obtained in the “away” direction, namely, from the foot point in the dayside ionosphere to the spacecraft altitude. The distribution of potentials for case 2 for the four spatial regions is shown in Figure 2d.

For photoelectrons/SWEA potential estimates only found in the “toward” direction (case 3), the most common scenario is cross-terminator closed field lines (e.g., Xu, Mitchell, et al., 2016). The distribution of the Mars potentials for this case is shown in Figure 2e. These potentials are from the dayside foot point to the spacecraft altitude. Dayside observations of case 3 can occur but not as frequent (the bottom panel of Figure S2) because of ambiguous “away” and “toward” directions (e.g., horizontal magnetic fields) or misidentifications from our technique. Therefore we omit the analysis of case 3 for dayside (Region 1).

Although the uncertainty for each measurement (1–2 V) is comparable to the value itself, the error in the mean is proportional to  $1/\sqrt{N}$ , where  $N$  is the total sample number for each distribution. Since  $N$  is  $\sim 10^5$ , the error in the mean is only a few hundredths of a volt. These distributions peak from  $-0.3$  to  $-1.2$  V, which is many times the standard error, indicating that our method yields mean potentials for the different topologies with a high degree of statistical significance.

These field-aligned potentials likely originate from the ambipolar electric field. First, our calculated average potential is negative from the ionospheric foot point to the spacecraft altitude, consistent with the ambipolar electric field direction, which retards electrons and accelerates ions. Second, the ambipolar electric field is typically on the order of  $\sim 1$  mV/km at Mars, which gives a potential difference 0.1–1 V over a few hundred-kilometer distance. Our calculated field-aligned potentials are of a similar magnitude.

The shapes of these distributions differ for a few possible reasons. First, field lines in different regions have different average geometries and thus tend to sample potential structures differently. For example, in Figures 2b–2e, there are higher percentages of more negative values when the spacecraft is tailward of the terminator ( $X < 0$ ), since field lines in that region with a foot point in the dayside ionosphere must cross the terminator, where the plasma density has a sharp gradient (Chapman, 1931a, 1931b), resulting in a relatively large potential drop. Field lines passing through the terminator thus sample a larger total potential drop. Additionally, superthermal electrons, though a small portion of the total electron density, have high velocities and can enhance or reduce the electron pressure gradient and thus affect the ambipolar electric field. As fluxes of superthermal electrons of both ionospheric and solar wind origin can vary significantly throughout the Mars environment, the contribution from these electrons to the total electron pressure gradient varies as well, broadening the distribution of field-aligned potentials differently.

Mean Mars potentials are mapped into cylindrical MSO coordinates in Figures 2f–2i. Median values (not shown) are very similar. A minimum sample number of 100 is imposed to ensure statistical significance. Mars potentials mostly vary from 0 to  $-1.5$  V, with standard errors  $< 0.05$  V. These potentials become more negative with increasing altitude on the dayside as the potential builds with distance from the electron exobase. The magnitude of the potential also increases with solar zenith angle (SZA), as the ambipolar electric field should be larger near the terminator because of the larger thermal density gradient. On the nightside, there is a sharp transition across the optical shadow ( $X < 0$ ,  $r_{\text{mso}} < 1 R_m$ ), with more negative potentials inside than outside, likely due to caveats A and C in Region 2. The results in this region should be taken with caution. Lastly, the few cells that show positive potentials remain on the outer edge, probably because both techniques have difficulties in the magnetic pileup and sheath region where the spacecraft potential mostly becomes near 0 or even positive.

#### 4.2. Dayside Potential Profiles

To facilitate ion escape, it is best for the field-aligned electric field to be located near the ion exobase ( $\sim 200$  km, ion mean free path approximately equals to neutral scale height), where the density is relatively high and ions can be accelerated upward without suffering too many collisions. Figure 3 shows Mars potential profiles (left column) and the derived electric fields (right column) on the dayside for closed and open field lines. In each panel, the calculated Mars potentials and electric fields are grouped into two SZA ranges,  $0\text{--}45^\circ$  (red) and  $45\text{--}90^\circ$  (blue).

Overall, below 800 km, the calculated Mars field-aligned potentials are near 0 at  $\sim 180$  km and grow to  $-0.4$  to  $-0.7$  V at 300 km and remain relatively constant above. Mars potentials on open field lines are slightly less negative with increasing altitude. It is probably because open field lines at higher altitudes are more likely to

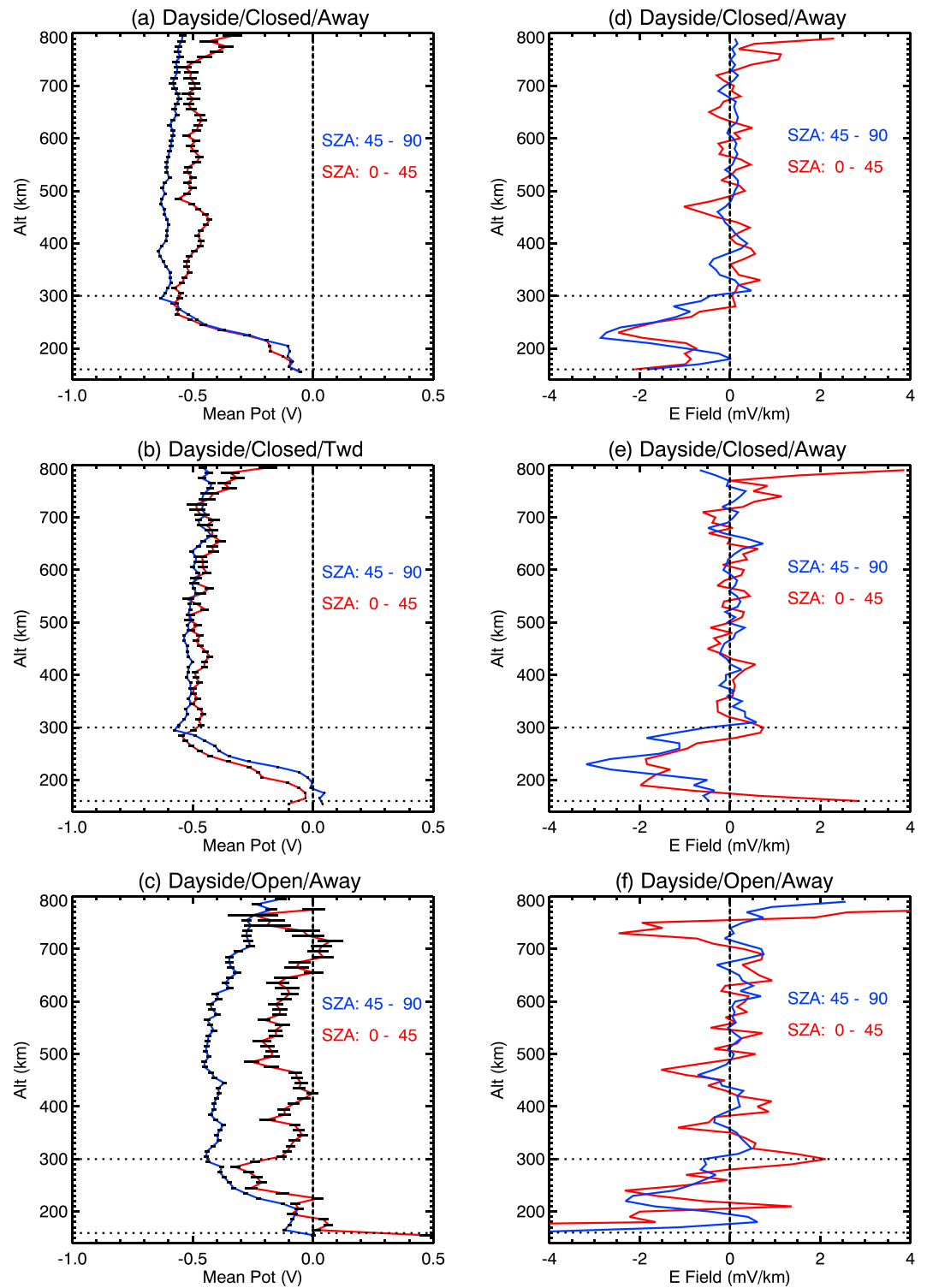


**Figure 3.** Three rows illustrate the dayside Mars potential profiles (the left column) and the derived electric fields (the right column) for closed-away, closed-toward, and open, respectively. In each panel, the red and blue lines are for SZA 0–45° and 45–90°, respectively. SZA = solar zenith angle.

have foot points at greater distances and lower SZAs than at the spacecraft, where the ambipolar potential is smaller. The irregularities in the profile for open field lines at SZA 0–45° (the red line in the bottom left panel) are possibly caused partly by not enough sampling to average over the ion bulk flow bias (caveat B).

The magnitude of field-aligned potentials display a smooth increase from ~180 to 300 km, indicating an electric field. We calculate this electric field using these averaged potential profiles, with the averaged magnetic dip angle applied to each altitude difference to convert to the delta distance along the field line. As shown in the right column of Figure 3, the calculated electric field mostly occurs between ~180 and 300 km, with a peak magnitude of 2–3 mV/km, consistent with the typical features of the ambipolar electric field. This electric field is located near the ion exobase, where it can enhance ion escape.

## 5. Discussion and Conclusions

Two independent potential estimates can be obtained from ionospheric photoelectron measurements from SWEA and ion observations from STATIC. STATIC provides an estimate of the spacecraft potential alone, while SWEA measures the combined spacecraft and Mars potentials. Mars field-aligned potentials are determined on various field topologies by taking the difference (SWEA-STATIC). By mapping into cylindrical MSO coordinates, average potentials are found to range from 0 to –1.5 V, with more negative values at high SZAs. The magnitude of these potentials is consistent with the upper limit determined by Collinson et al. (2015).

These field-aligned potentials are found on both closed and open field lines, of a similar magnitude to and consistent with the direction of the ambipolar electric field. The measured field-aligned potentials also have a SZA dependence that can be explained by a larger ambipolar electric field near the terminator due to a larger plasma pressure gradient. The calculated electric field is of a similar magnitude (0–3 mV/km) and located in a region similar to the ambipolar electric field driven by the plasma pressure gradient. Thus, we interpret these field-aligned potentials as a result of the ambipolar electric field.

Below 800 km, the average dayside Mars potentials are found to be mostly between 0 and –0.7 V. The escaping energies for O<sub>2</sub><sup>+</sup> and O<sup>+</sup> are 4 and 2 V, respectively. It means that these potentials are able to shift the ion distribution to higher energy and enhance ion outflow (analogous to Jeans escape; e.g., Moore & Khazanov, 2010), as noted by Collinson et al. (2015). In addition, the derived electric fields are mostly located 180–300 km, right near the ion exobase, where they are most effective at enhancing ion outflow.

## Acknowledgments

This work was supported by the National Aeronautics and Space Administration (NASA) grant NNN10CC04C to the University of Colorado and by subcontract to Space Sciences Laboratory, University of California, Berkeley. The MAVEN project is supported by NASA through the Mars Exploration Program. The MAVEN data used in this study are available through Planetary Data System (<http://ppi.pds.nasa.gov/mission/MAVEN>).

## References

- Banks, P. M., & Holzer, T. E. (1968). The polar wind. *Journal of Geophysical Research*, 73(21), 6846–6854.
- Bougher, S., Engel, S., Roble, R., & Foster, B. (2000). Comparative terrestrial planet thermospheres: 3. Solar cycle variation of global structure and winds at solstices. *Journal of Geophysical Research*, 105(E7), 17,669–17,692.
- Bougher, S., Pawlowski, D., Bell, J., Nelli, S., McDunn, T., Murphy, J., et al. (2015). Mars Global Ionosphere-Thermosphere Model: Solar cycle, seasonal, and diurnal variations of the Mars upper atmosphere. *Journal of Geophysical Research: Planets*, 120, 311–342. <https://doi.org/10.1002/2014JE004715>
- Chapman, S. (1931a). The absorption and dissociative or ionizing effect of monochromatic radiation in an atmosphere on a rotating Earth. *Proceedings of the Physical Society*, 43, 26–45. <https://doi.org/10.1088/0959-5309/43/1/305>
- Chapman, S. (1931b). The absorption and dissociative or ionizing effect of monochromatic radiation in an atmosphere on a rotating Earth Part II. Grazing incidence. *Proceedings of the Physical Society*, 43, 483–501. <https://doi.org/10.1088/0959-5309/43/5/302>
- Collinson, G. A., Frahm, R. A., Glocer, A., Coates, A. J., Grebowsky, J. M., Barabash, S., et al. (2016). The electric wind of Venus: A global and persistent “polar wind”-like ambipolar electric field sufficient for the direct escape of heavy ionospheric ions. *Geophysical Research Letters*, 43, 5926–5934. <https://doi.org/10.1002/2016GL068327>
- Collinson, G., Mitchell, D., Glocer, A., Grebowsky, J., Peterson, W. K., Connerney, J., et al. (2015). Electric Mars: The first direct measurement of an upper limit for the Martian “polar wind” electric potential. *Geophysical Research Letters*, 42, 9128–9134. <https://doi.org/10.1002/2015GL065084>
- Collinson, G., Mitchell, D., Xu, S., Glocer, A., Grebowsky, J., Hara, T., et al. (2016). Electric Mars: A large trans-terminator electric potential drop on closed magnetic field lines above Utopia Planitia. *Journal of Geophysical Research: Space Physics*, 122, 2260–2271. <https://doi.org/10.1002/2016JA023589>
- Connerney, J., Easley, J., Lawton, P., Murphy, S., Odom, J., Oliverson, R., & Sheppard, D. (2015). The MAVEN magnetic field investigation. *Space Science Reviews*, 195, 257–291.
- Ergun, R. E., Andersson, L. A., Fowler, C. M., Woodson, A. K., Weber, T. D., Delory, G. T., et al. (2016). Enhanced O<sub>2</sub><sup>+</sup> loss at Mars due to an ambipolar electric field from electron heating. *Journal of Geophysical Research: Space Physics*, 121, 4668–4678. <https://doi.org/10.1002/2016JA022349>
- Ganguli, S. B. (1996). The polar wind. *Reviews of Geophysics*, 34(3), 311–348. <https://doi.org/10.1029/96RG00497>
- Glocer, A., Khazanov, G., & Liemohn, M. (2017). Photoelectrons in the quiet polar wind. *Journal of Geophysical Research: Space Physics*, 122, 6708–6726. <https://doi.org/10.1002/2017JA024177>
- Jakosky, B., Brain, D., Chaffin, M., Curry, S., Deighan, J., Grebowsky, J., et al. (2018). Loss of the Martian atmosphere to space: Present-day loss rates determined from MAVEN observations and integrated loss through time. *Icarus*, 315, 146–157. <https://doi.org/10.1016/j.icarus.2018.05.030>

- Jakosky, B. M., Lin, R., Grebowsky, J., Luhmann, J., Mitchell, D., Beutelschies, G., et al. (2015). The Mars Atmosphere and Volatile Evolution (MAVEN) mission. *Space Science Reviews*, 195(1-4), 3–48.
- Khazanov, G., Liemohn, M., Krivovrutsky, E., & Moore, T. (1998). Generalized kinetic description of a plasma in an arbitrary field-aligned potential energy structure. *Journal of Geophysical Research*, 103(A4), 6871–6889.
- Khazanov, G. V., Liemohn, M. W., & Moore, T. E. (1997). Photoelectron effects on the self-consistent potential in the collisionless polar wind. *Journal of Geophysical Research*, 102(A4), 7509–7521. <https://doi.org/10.1029/96JA03343>
- Kitamura, N., Seki, K., Nishimura, Y., & McFadden, J. P. (2015). Limited impact of escaping photoelectrons on the terrestrial polar wind flux in the polar cap. *Geophysical Research Letters*, 42, 3106–3113. <https://doi.org/10.1002/2015GL063452>
- Kitamura, N., Seki, K., Nishimura, Y., Terada, N., Ono, T., Hori, T., & Strangeway, R. J. (2012). Photoelectron flows in the polar wind during geomagnetically quiet periods. *Journal of Geophysical Research*, 117, A017459. <https://doi.org/10.1029/2011JA017459>
- Liemohn, M. W., Mitchell, D. L., Nagy, A. F., Fox, J. L., Reimer, T. W., & Ma, Y. (2003). Comparisons of electron fluxes measured in the crustal fields at Mars by the MGS magnetometer/electron reflectometer instrument with a B field–dependent transport code. *Journal of Geophysical Research*, 108(E12), 5134. <https://doi.org/10.1029/2003JE002158>
- Lillis, R. J., Brain, D. A., Bougher, S. W., Leblanc, F., Luhmann, J. G., Jakosky, B. M., et al. (2015). Characterizing atmospheric escape from Mars today and through time, with MAVEN. *Space Science Reviews*, 195(1-4), 357–422.
- Lillis, R. J., Halekas, J., Fillingim, M., Poppe, A., Collinson, G., Brain, D. A., & Mitchell, D. (2018). Field-aligned electrostatic potentials above the Martian exobase from MGS electron reflectometry: Structure and variability. *Journal of Geophysical Research: Planets*, 123, 67–92. <https://doi.org/10.1002/2017JE005395>
- Mantas, G. P., & Hanson, W. B. (1979). Photoelectron fluxes in the Martian ionosphere. *Journal of Geophysical Research*, 84(A2), 369–385. <https://doi.org/10.1029/JA084iA02p00369>
- McFadden, J., Kortmann, O., Curtis, D., Dalton, G., Johnson, G., Abiad, R., et al. (2015). MAVEN SupraThermal And Thermal Ion Composition (STATIC) instrument. *Space Science Reviews*, 195(1-4), 199–256.
- Mitchell, D., Lin, R., Reme, H., Crider, D., Cloutier, P., Connerney, J., et al. (2000). Oxygen Auger electrons observed in Mars' ionosphere. *Geophysical research letters*, 27(13), 1871–1874.
- Mitchell, D., Mazelle, C., Sauvaud, J.-A., Thocaven, J.-J., Rouzaud, J., Fedorov, A., et al. (2016). The MAVEN Solar Wind Electron Analyzer. *Space Science Reviews*, 200(1-4), 495–528.
- Moore, T. E., & Khazanov, G. V. (2010). Mechanisms of ionospheric mass escape. *Journal of Geophysical Research*, 115, A00J13. <https://doi.org/10.1029/2009JA014905>
- Peterson, W., Thiemann, E., Eparvier, F. G., Andersson, L., Fowler, C., Larson, D., et al. (2016). Photoelectrons and solar ionizing radiation at Mars: Predictions versus MAVEN observations. *Journal of Geophysical Research: Space Physics*, 121, 8859–8870. <https://doi.org/10.1002/2016JA022677>
- Schunk, R. W. (1988). The polar wind. *Modeling Magnetospheric Plasma* (Vol. 44, pp. 219–228). Washington, DC: American Geophysical Union.
- Schunk, R., & Nagy, A. (2009). *Ionospheres*. Cambridge: Cambridge University Press.
- Welling, D. T., André, M., Dandouras, I., Delcourt, F., Fazakerley, A., Fontaine, D., et al. (2015). The Earth: Plasma sources, losses, and transport processes. *Space Science Reviews*, 192(1-4), 145–208.
- Xu, S., Fang, X., Mitchell, D. L., Ma, Y., Luhmann, J. G., DiBraccio, G. A., et al. (2018). Investigation of Martian magnetic topology response to 2017 September ICME. *Geophysical Research Letters*, 45, 7337–7346. <https://doi.org/10.1029/2018GL077708>
- Xu, S., & Liemohn, M. W. (2015). Superthermal electron transport model for Mars. *Earth and Space Science*, 2, 47–64. <https://doi.org/10.1002/2014EA000043>
- Xu, S., Liemohn, M., Bougher, S., & Mitchell, D. (2015). Enhanced carbon dioxide causing the dust storm-related increase in high-altitude photoelectron fluxes at Mars. *Geophysical Research Letters*, 42, 9702–9710. <https://doi.org/10.1002/2015GL066043>
- Xu, S., Liemohn, M., Bougher, S., & Mitchell, D. (2016). Martian high-altitude photoelectrons independent of solar zenith angle. *Journal of Geophysical Research: Space Physics*, 121, 3767–3780. <https://doi.org/10.1002/2015JA022149>
- Xu, S., Liemohn, M. W., & Mitchell, D. L. (2014). Solar wind electron precipitation into the dayside Martian upper atmosphere through the cusps of strong crustal fields. *Journal of Geophysical Research: Space Physics*, 119, 10,100–10,115. <https://doi.org/10.1002/2014JA020363>
- Xu, S., Liemohn, M. W., Peterson, W., Fontenla, J., & Chamberlin, P. (2015). Comparison of different solar irradiance models for the superthermal electron transport model for Mars. *Planetary and Space Science*, 119, 62–68.
- Xu, S., Mitchell, D., Liemohn, M., Dong, C., Bougher, S., Fillingim, M., et al. (2016). Deep nightside photoelectron observations by MAVEN SWEA: Implications for Martian northern hemispheric magnetic topology and nightside ionosphere source. *Geophysical Research Letters*, 43, 8876–8884. <https://doi.org/10.1002/2016GL070527>
- Xu, S., Mitchell, D., Liemohn, M., Fang, X., Ma, Y., Luhmann, J., et al. (2017). Martian low-altitude magnetic topology deduced from MAVEN/SWEA observations. *Journal of Geophysical Research: Space Physics*, 122, 1831–1852. <https://doi.org/10.1002/2016JA023467>
- Xu, S., Mitchell, D., Luhmann, J., Ma, Y., Fang, X., Harada, Y., et al. (2017). High-altitude closed magnetic loops at Mars observed by MAVEN. *Geophysical Research Letters*, 44, 11,229–11,238. <https://doi.org/10.1002/2017GL075831>
- Xu, S., Thiemann, E., Mitchell, D., Eparvier, F., Pawlowski, D., Benna, M., et al. (2018). Observations and modeling of the Mars low-altitude ionospheric response to the 10 September 2017 X-Class solar flare. *Geophysical Research Letters*, 45, 7382–7390. <https://doi.org/10.1029/2018GL078524>
- Yau, A. W., Abe, T., & Peterson, W. (2007). The polar wind: Recent observations. *Journal of Atmospheric and Solar-Terrestrial Physics*, 69(16), 1936–1983. <https://doi.org/10.1016/j.jastp.2007.08.010>, recent Advances in the Polar Wind Theories and Observations.

## Erratum

In the originally published version of this article, the legends for Figures 1 and 2 were transposed. As a result, the references to these figures in text were also published incorrectly. These errors have since been corrected, and this version may be considered the authoritative version of record.